

Master's Degree in Electrical and Computer Engineering

Laboratory work
COMPUTER CONTROL

**Identification and Computer Control
of a Flexible Robot Arm Joint**

PART II

Authors: João Prata 69933
Luís Rei 78486
João Girão 78761

December 19, 2017

Contents

List of Tables	ii
List of Figures	ii
1 Introduction	1
2 Controller Design (Question 4)	1
2.1 Linear-Quadratic Control Law	2
2.2 Kalman Filter	9
2.3 Loop Transfer Recovery	10
2.4 Linear-Quadratic-Gaussian Controller Structure	14
3 Experimental Results	17
3.1 Dealing with the Dead Zone	20

List of Tables

1	Parameters' variation using method 2 with Q_w/R_v ratio = 1000.	11
2	Parameters' variation using method 1 with different ratios.	12
3	Parameters' variation using method 2 with different ratios.	12

List of Figures

1	System model.	2
2	State-feedback controller.	3
3	Time response of the closed-loop system.	3
4	Logarithmic time response of the closed-loop system.	4
5	Frequency response of the loop transfer function.	4
6	Logarithmic time response with $R = 100$	5
7	Time response decay rate with $R = 100$	5
8	Logarithmic time response with $R = 0$	6
9	Time response decay rate with $R = 0$	6
10	Closed-loop system.	7
11	Frequency response of the closed-loop system.	7
12	Closed-loop LQR (left) and open-loop LQR (right) zero/pole analysis in the complex plane.	8
13	Closed-loop poles evolution by varying R	8
14	Root-locus analysis (left) and symmetric poles for $R=100$ (right).	9
15	Block diagram of the state estimator. The part in red corresponds to the predictive observer and the part in blue to the correction to obtain the current estimate $\hat{x}(k)$. . .	10
16	Linear-Quadratic Estimator.	11
17	Time response with Q_w/R_v ratio = 1000 using method 1 (left) and method 2 (right). .	11
18	Pole locations with Q_w/R_v ratio = 1000 using method 1 (left) and method 2 (right). .	12
19	Time response with different Q_w/R_v ratios using method 1 (left) and method 2 (right). .	12
20	Pole locations for varying ρ_v using method 1. Open-loop system at left and closed-loop at the right.	13
21	Pole locations for varying ρ_v using method 2. Open-loop system at left and closed-loop at the right.	13
22	Joint system.	14
23	Open-loop transfer function using method's 1 (right) and method's 2 loop-gains (right). .	14
24	Closed-loop frequency response comparison between LQR and LQG controller. . . .	15
25	Closed-loop pole cancellation (left) and linear state feedback and estimator poles (right) for $Q_w = 100I$ and $R_v = 1$	15
26	Root-locus analysis (left) and symmetric poles for $Q_w = 100I$ and $R_v = 1$ (right). . .	16
27	Closed-loop LQG pole cancellation (left) and closed-loop LQR (right).	16
28	Diagram used on the real plant tests.	17
29	Square signal response with frequency of $0.2 [Hz]$, with parameters $Q_w = 100I$, $R_v = 1$ (LQE) and $R = 100$ (LQR). Response without perturbances (left) and with perturbances (right).	17
30	Square signal response with a frequency of $0.6 [Hz]$	18
31	Square signal response with $Q_w = 100I$, $R_v = 1$ (LQE) and $R = 200$ (LQR). Response without perturbances (left) and with perturbances (right).	18
32	Square signal response with $Q_w = 100I$, $R_v = 20$ (LQE) and $R = 100$ (LQR). Response without perturbances (left) and with perturbances (right).	19
33	Sawtooth signal response with $Q_w = 100I$, $R_v = 1$ (LQE) and $R = 100$ (LQR).	19

34	Simulink diagram able to deal with the dead zone imposed by the motor.	20
35	System's time response to step signal, with varying τ	20
36	Time response to square signal, dealing with dead zone with $\tau = 0.1$. Signal without perturbances (left) and with perturbances (right).	21
37	Time response to sawtooth signal without perturbances, dealing with dead zone with $\tau = 0.1$	21
38	Joint system without reset level on the integrator.	22
39	Time response to square signal without perturbances (left) and to the sawtooth signal with one perturbation (right) without the integrator's reset, with $\tau = 0.1$	22
40	Robust system with selector of reset level.	23

1 Introduction

In this report, the state-space model identified described on the previous stage of the laboratory work is used to design a linear–quadratic–Gaussian (LQG) controller, a combination of a Kalman filter, i.e. a linear–quadratic estimator (LQE), with a linear–quadratic regulator (LQR). The separation principle guarantees that these can be designed and computed independently.

After testing the controller in a simulation environment several choices of the weights on a quadratic cost when using the LQG design approach are explored. The effect of the choice of the noise covariance matrices in a Loop transfer recovery (LTR) framework and the resulting closed-loop frequency response and time response is examined. After calculating the loop-gain, a discussion on how to evaluate the performance of the control system and what are the limits of performance is ensued.

2 Controller Design (Question 4)

The state-space model identified described on part 1 of the project used to design a LQG controller is given by

$$A = \begin{bmatrix} 3.3417 & -4.3177 & 2.5739 & -0.5979 \\ 1.0000 & 0 & 0 & 0 \\ 0 & 1.0000 & 0 & 0 \\ 0 & 0 & 1.0000 & 0 \end{bmatrix}, \quad B = \begin{bmatrix} 1 \\ 0 \\ 0 \\ 0 \end{bmatrix},$$
$$C = [-0.0615 \quad 0.1169 \quad 0 \quad 0], \quad D = 0.$$

The controller consists of a state feedback control law whose gains are selected such as to minimize a quadratic cost on the basis of the state model 1a, 1b that has been identified (section 2.1).

$$x(k+1) = Ax(k) + Bu(k), \quad (1a)$$

$$y(k) = Cx(k) + Du(k). \quad (1b)$$

Since we do not have access to the state of the plant, a Kalman filter is estimated to combat that limitation (section 2.2). The Kalman filter receives as input the plant input and output, and yields as it output an estimate of the plant state. The filter's structure is equal to the current observer, but its gain is selected in a particular way so as to optimize the signal-to-noise ratio of the estimate in the presence of noise that affects the plant (optimal design of the parameters).

The control of the flexible bar project will be done in a two-phased process:

1. firstly, in a simulation environment, the design and validation of a controller and observer, and posterior joint system, is done (loop transfer functions, stability margins, and settling times will be analyzed);
2. secondly, and after testing the effect of an external input in simulation, tests on the real system are performed.

This design process will be repeated until satisfactory results are obtained.

2.1 Linear-Quadratic Control Law

The control law that generates the manipulated variable u for the state model seen in 1a, 1b such as to minimize the steady-state quadratic cost

$$J = \sum_{k=1}^{\infty} x^T(k) Q x(k) + u^T(k) R u(k), \quad (2)$$

where Q is positive semi-definite and R is positive definite is given by the state feedback

$$u(k) = -Kx(k), \quad (3)$$

where the vector of feedback gains K is computed by

$$K = (B^T S B + R)^{-1} B^T S A. \quad (4)$$

If there exists a K such that the closed-loop system that results from coupling 1a with 3 minimizes the cost 2, then it can be found by 4 and following the only positive definite solution (matrix S) of the algebraic Riccati equation (ARE)

$$A^T S A - A^T S B (B^T S B + R)^{-1} B^T S A + Q = 0. \quad (5)$$

The main “tuning knob” for the designer when using LQ control are the matrices Q and R . For a SISO plant, if the output y is to be regulated then, due to 1a and $D = 0$,

$$Q = C^T C. \quad (6)$$

With $Q = H^T H$, $y^2(k) = (x^T(k) H^T)(H x(k))$, and taking into account $R = \frac{1}{rho}$, we get the optimal linear quadratic regulator (LQR) given by

$$J(k) = \sum_{k=0}^{\infty} (y^2(k) + \frac{1}{\rho} u^2(k)). \quad (7)$$

With Q leading the state to zero, the regulator problem with no external input tries to find balance on conflictive objectives. Changing R (now reduced to a scalar) adjusts the type of response yielded as it penalizes the control applied to the system - it represents how much energy we use so we achieve our goal. In general, decreasing R increases the bandwidth of the control system, providing a “cheap” control with a nervous behavior as the closed-loop poles tend to their asymptotic position (stable roots of the root square locus). Decreasing R has the advantage of making the response of the close loop faster (R is dominant), but the disadvantage of exciting plant modes that are not modeled. Increasing R leads to a more expensive control; the stable poles in the complex plane are in the initial conditions.

From the system model in 1, described in 8a and 8b,

$$x(k+1) = \Phi x(k) + \Gamma u(k), \quad (8a)$$

$$y(k) = H x(k). \quad (8b)$$

and following the design strategy mentioned before, analyzing the state-feedback controller in 2 we determine the optimal parameter to suit our needs.

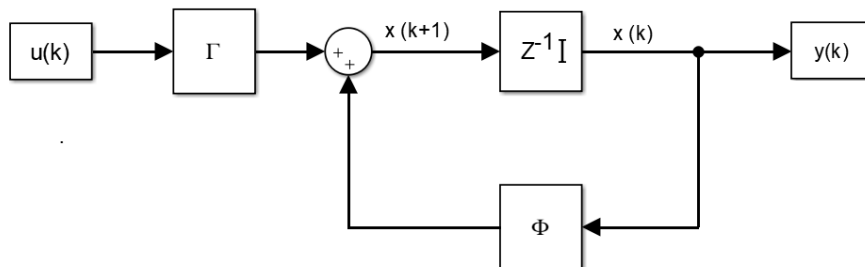


Figure 1: System model.

To better understand the influence of the poles we analyse the logarithmic response of the system in figure 4.

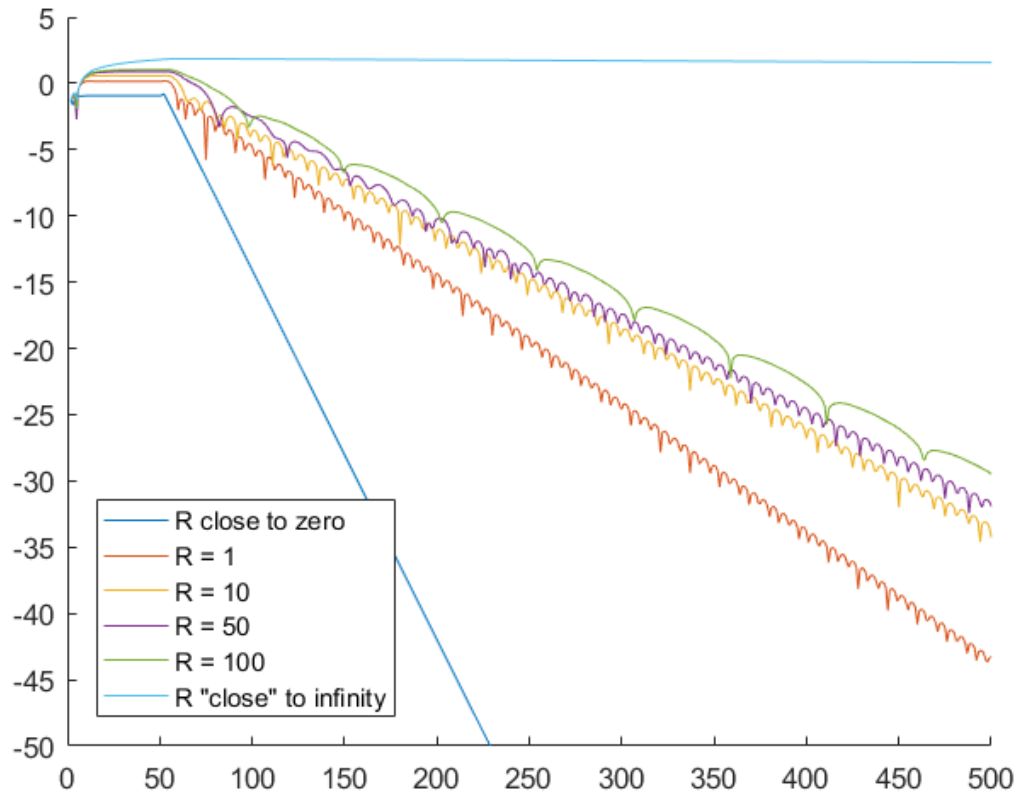


Figure 4: Logarithmic time response of the closed-loop system.

The loop transfer function may be described by a discrete state-space model with input Γ , dynamic matrix Φ and output vector K . The frequency response can be obtained as shown in figure 5 for relevant values of R .

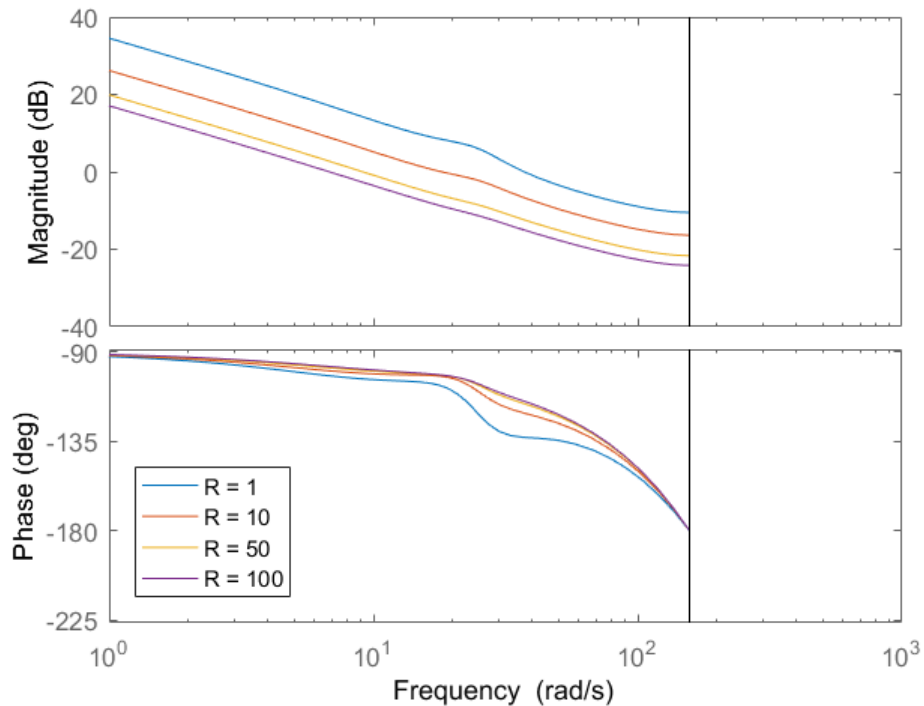


Figure 5: Frequency response of the loop transfer function.

Selecting a conservative $R = 100$, we assess the decay rate of the (logarithmic) time response in figure 6 and take a closer look into the decay rate according to the absolute value of the biggest eigenvalue of the system - eigenvalues of $(\Phi - \Gamma K)$.

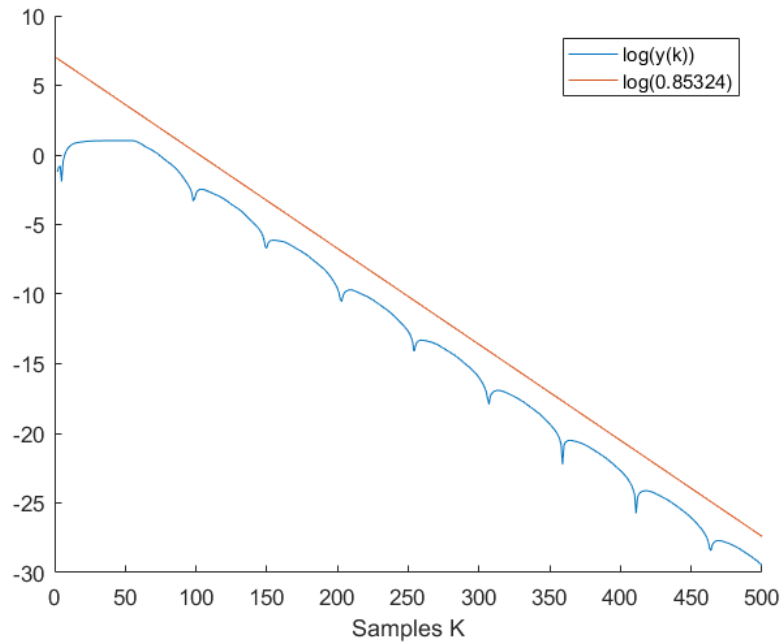


Figure 6: Logarithmic time response with $R = 100$.

Through observation we observe the impact of non-dominant poles in the system. With decay $h(k) = \sum_i h_i \lambda_i^k$, where λ_i are the closed-loop poles, and observing the slope of the response in figure 6 we conclude that the poles of the modeled system are not in the optimal positions as we see an offset between the red and blue lines. Under these conditions, and due to the closeness of the absolute values of the eigenvalues of $(\Phi - \Gamma K)$ (figure 7), our conclusions are uncertain on whether our validation was well executed. In the following figure the expected response of the system is seen represented by the dotted pattern, while the biggest eigenvalue is done with a dashed plot.

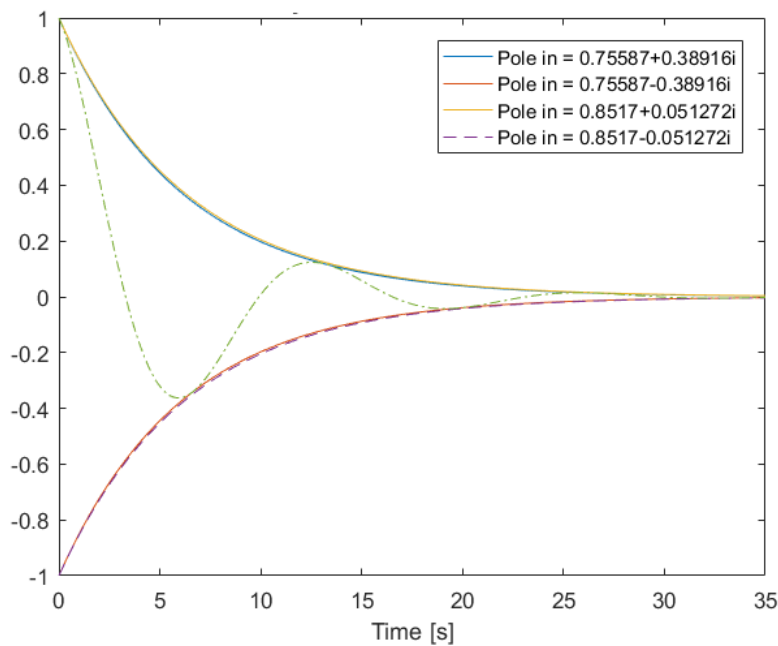


Figure 7: Time response decay rate with $R = 100$.

To vaporize any doubts we ensued an evaluation of the same kind but with R close to zero, as in these setup a dominant pole will be guaranteed to be present and the slope of the logarithmic response is expected to follow the logarithmic time response of the system.

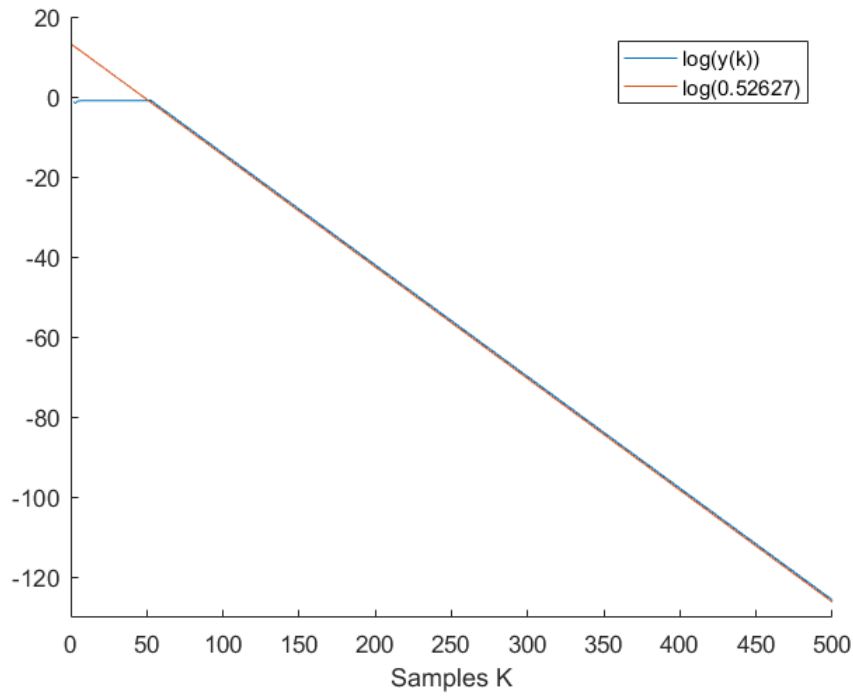


Figure 8: Logarithmic time response with $R = 0$.

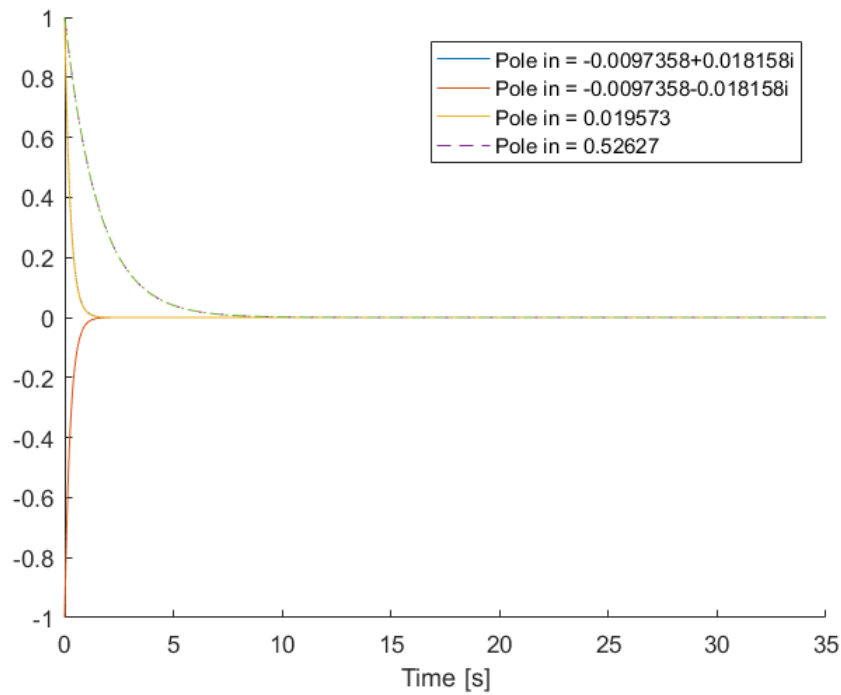


Figure 9: Time response decay rate with $R = 0$.

Figures 8 and 9 confirm the correctness of our solution through the analysis of the decay rates.

For the closed-loop frequency response we first compute the gain for the external input that will lead the gain of the system between the reference and the output to be unitary. Realizing the closed-loop system (figure 10) the bode diagram is presented in figure 11 showcasing the same values of R as previously seen in figure 5.

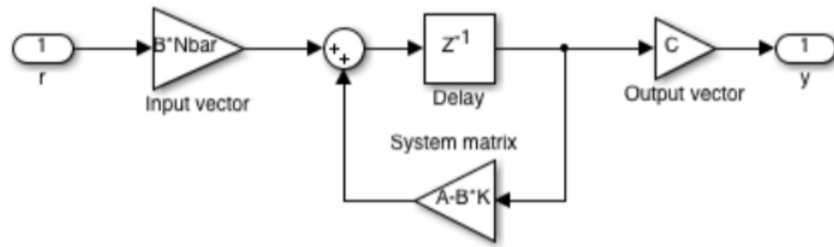


Figure 10: Closed-loop system.

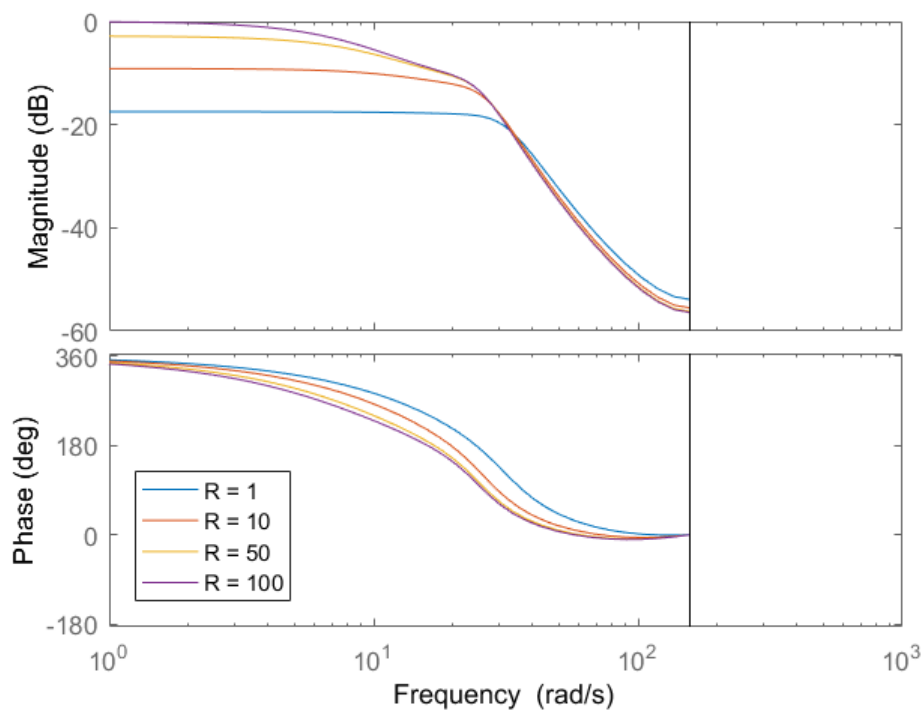


Figure 11: Frequency response of the closed-loop system.

Note that the closed-loop poles match, up to a permutation, the ones observed in part 1 of the laboratory work (figure 12).

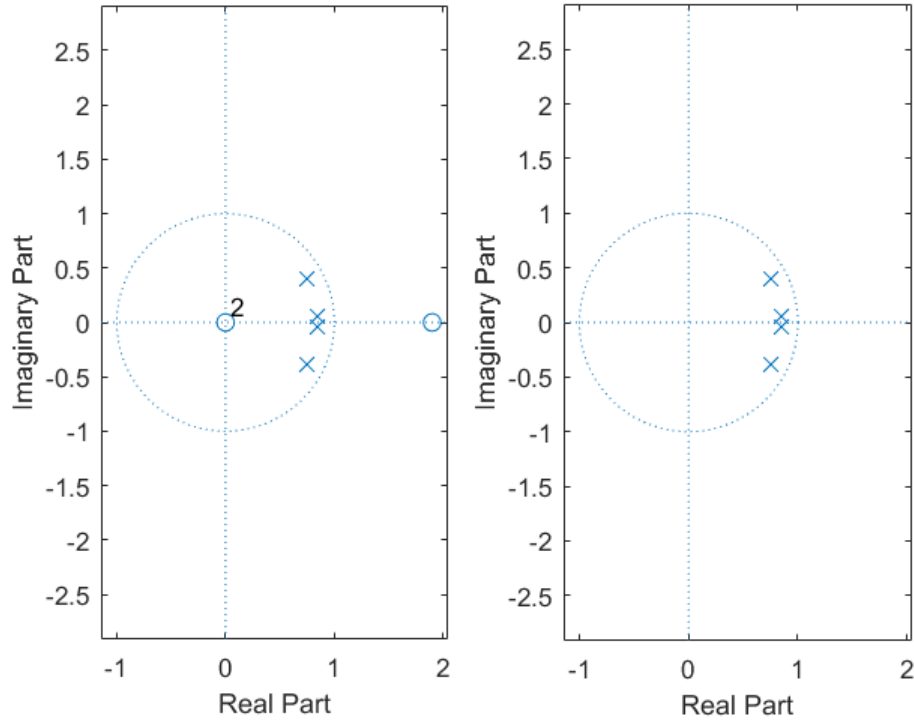


Figure 12: Closed-loop LQR (left) and open-loop LQR (right) zero/pole analysis in the complex plane.

The designed regulator has a feedback gain of

$$K = \begin{bmatrix} 0.1266 & -0.2918 & 0.2421 & -0.0717 \end{bmatrix}. \quad (9)$$

Scanning through several R values the poles evolution seen in figure 13 is built.

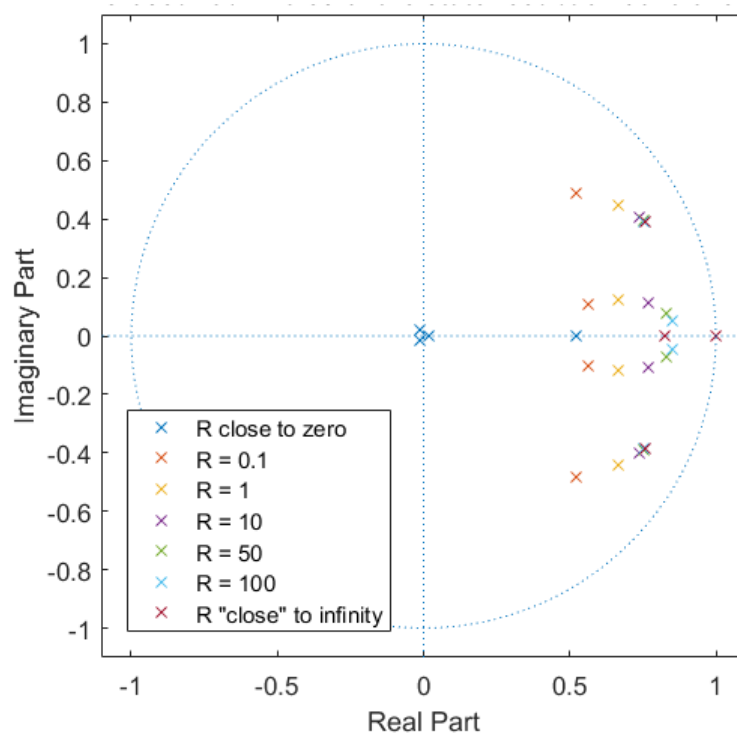


Figure 13: Closed-loop poles evolution by varying R .

Using a technique known as root-square locus (figure 14) the overall picture of the dependence of the closed-loop poles on R is enlightened even further. The symmetric poles are visible in the same figure.

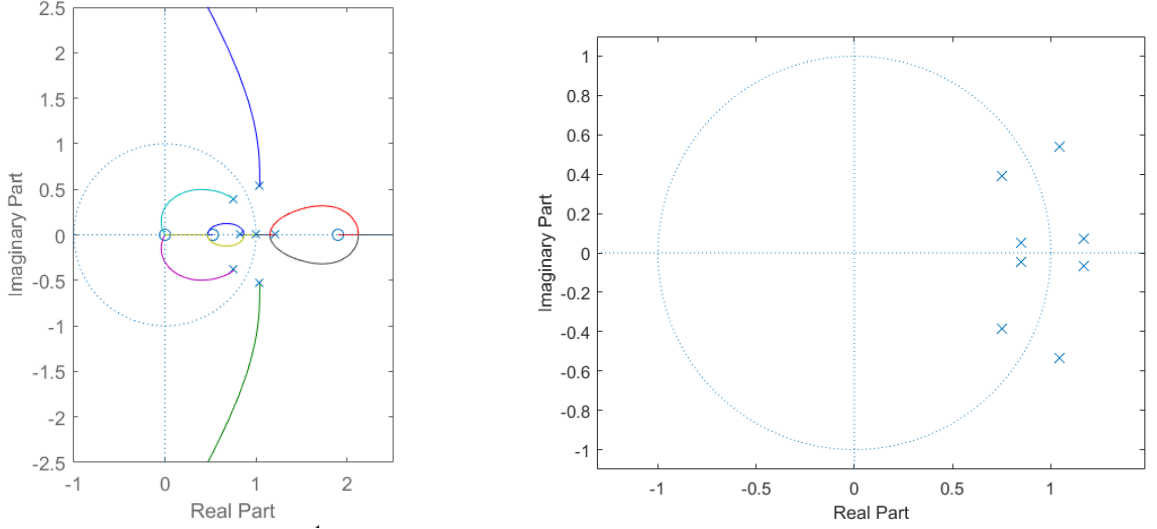


Figure 14: Root-locus analysis (left) and symmetric poles for $R=100$ (right).

Note that the closed-loop poles are the stable roots of

$$1 + \rho G(Z)G(Z^{-1}) = 0. \quad (10)$$

In our system, $G(Z)$ has a zero in $z = 0$ and other two zeros at infinity, because $G(Z)$ converges to 0 with $1/z^2$ when $z \rightarrow \text{inf}$. These zeros switch position in $G(z^{-1})$, making two zeros appear at the origin (converges to 0 with $1/z$ when $z \rightarrow \text{inf}$). In sum, $G(z)G(z^{-1})$ has three zeros at the origin. Counting the other pairs of reciprocate poles/zeros we have a total of 5 zeros and 8 poles, which matches the 3 asymptotes that we witness in the root-locus of figure 14.

2.2 Kalman Filter

The Kalman filter aims at estimating the plant state from the observation of the plant input and output and assumes that the plant model is modified by the inclusion of “disturbance” or “noise” inputs, becoming

$$x(k+1) = \Phi x(k) + \Gamma u(k) + \Gamma_1 w(k), \quad (11a)$$

$$y(k) = Hx(k) + v(k). \quad (11b)$$

Note that we now declare

$$J'(L) = \sum_{k=0}^{\infty} (x(k) - \hat{x}(k))^2. \quad (12)$$

The signal \mathbf{w} is the process noise, that models random disturbances and whose covariance will be given by Q_w , and the signal is the sensor noise. The Kalman filter has the structure of the current observer (figure 15), with the gain optimized by taking into account these noise terms. The signal \mathbf{v} constitutes the observation noise, whose covariance is denoted R_v .

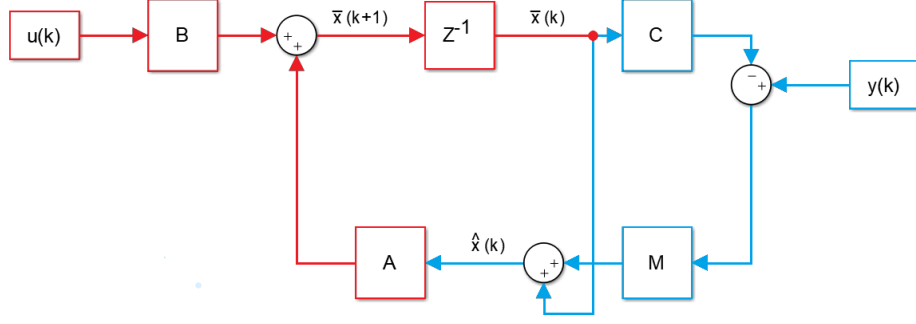


Figure 15: Block diagram of the state estimator. The part in red corresponds to the predictive observer and the part in blue to the correction to obtain the current estimate $\hat{x}(k)$.

The equations of the Kalman filter (current observer) are given by

$$\hat{x}(k|k-1) = \Phi\hat{x}(k-1|k-1) + \Gamma u(k|k-1), \quad (13a)$$

$$\hat{x}(k|k) = \hat{x}(k-1|k-1) + M(y(k) - C\hat{x}(k|k-1)). \quad (13b)$$

Equation 13a computes what you expect the state to be at time k given the previous estimate $\hat{x}(k-1|k-1)$, the input sample applied, $u(k-1)$, and the knowledge about the state dynamics. Then, this prediction is corrected by a term that is proportional to what you expect the output to be given the state prediction, $C\hat{x}(k|k-1)$, and what is actually observed for the value of $y(k)$. The proportionality constant vector is called the Kalman gain.

2.3 Loop Transfer Recovery

The computation of the Kalman gain requires the covariance matrices of the noises entering the model. These are $Q_w = \varepsilon(ww^T)$ and $R_v = \varepsilon(vv^T)$ (this last one a scalar). Instead of trying to estimate these noise covariances from plant data, we are going to use them as “tuning knobs”. Two methodologies are attempted during this phase of the work:

1. Method 1 assumes the configuration just explained, with $Q_w = q_w I$, $\Gamma_1 = I$ and R_v a scalar;
2. Method 2 locks $Q_w = 1$, assumes $\Gamma_1 = \Gamma = B$ and uses R_v (inverse of ρ_v) as a tuning knob, allowing a similar analysis to what was done in the previous section regarding the controller design.

In this second approach an increase in ρ_v translates in a more reliable output, but with a nervous observer. In contrast, a lower value of the parameter provides a noisy output and translates in a slow observer response.

Using the block diagram in figure 16 the design and validation of the observer is achieved.

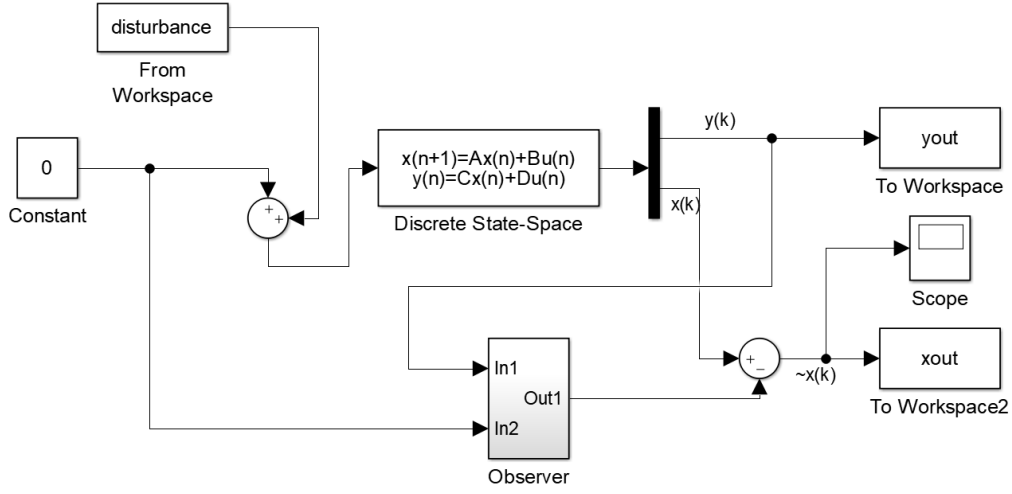


Figure 16: Linear-Quadratic Estimator.

In this section we provide an analysis on both methods and confirm if their theoretical similarities translate into an equal practical behavior. Maintaining the Q_w/R_v ratio locked to a constant (table 1) we observe the respective time responses (figure 17).

Table 1: Parameters' variation using method 2 with Q_w/R_v ratio = 1000.

Q_w	R_v
10	0.01
100	0.1
1000	1
10000	10

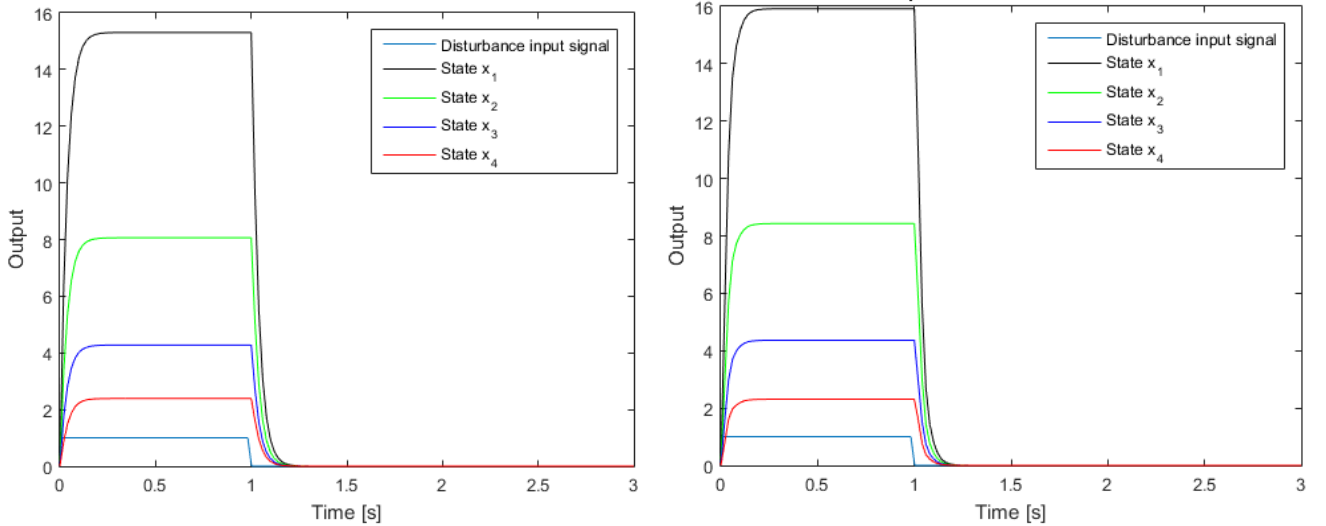


Figure 17: Time response with Q_w/R_v ratio = 1000 using method 1 (left) and method 2 (right).

Qualitatively we witness the same state convergence behavior. Do note that method 2 provides an output that has a slightly higher ceiling than method 1. The pole locations for this particular time response is shown in figures 18.

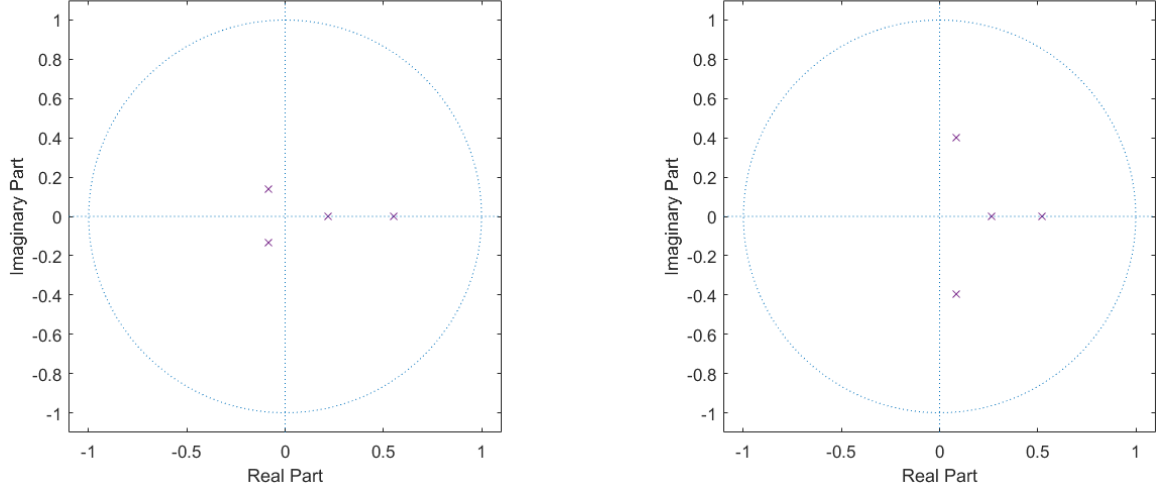


Figure 18: Pole locations with Q_w/R_v ratio = 1000 using method 1 (left) and method 2 (right).

Experimenting with different ratios, as seen in tables 2 and 3, outputs new time responses (figure 19).

Table 2: Parameters' variation using method 1 with different ratios.

Q_w	R_v	Ratio
100 I	0.01	10000
100 I	0.1	1000
100 I	1	100
100 I	10	10

Table 3: Parameters' variation using method 2 with different ratios.

Q_w	R_v	Ratio
1	0.0001	10000
1	0.001	1000
1	0.01	100

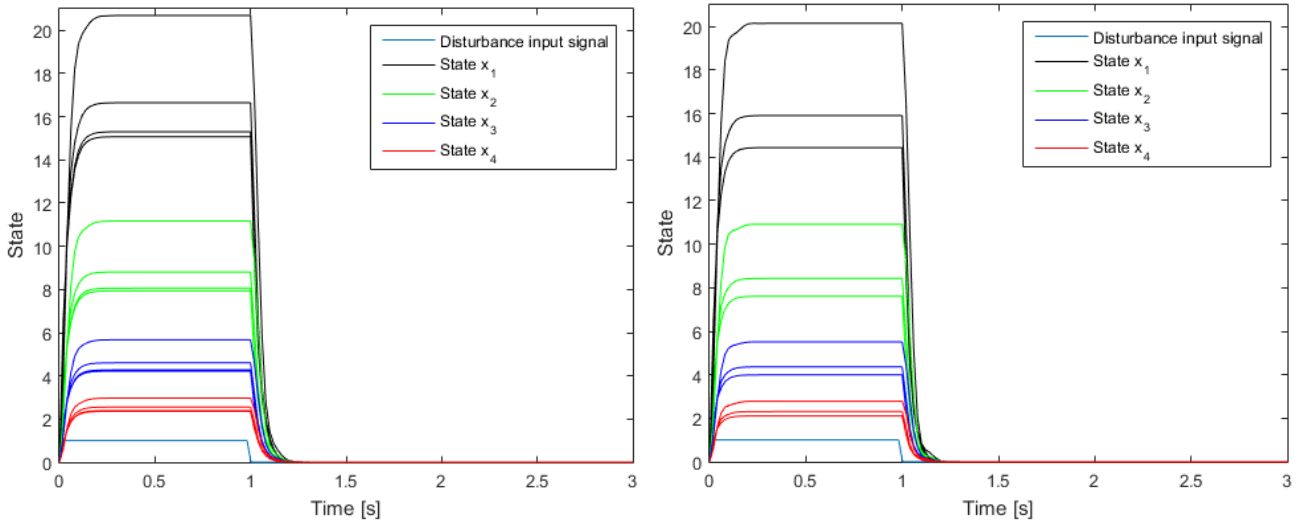


Figure 19: Time response with different Q_w/R_v ratios using method 1 (left) and method 2 (right).

Again, performing a qualitative analysis we conclude that their behavior is equal, despite the slight variation in the states peak value between the two methods. After examining the eigenvalues of $(\Phi - L_c H \Phi)$ we conclude the decay rate observed was consistent with the system. As the ratio decreases the states' peak value increases with both methods.

To check the consistency of the closed-loop poles using method 1 we lock Q_w to 100I and vary ρ_v accordingly (figure 20). An overall picture of the dependence of the error equation poles of the observer on R_v is attained.

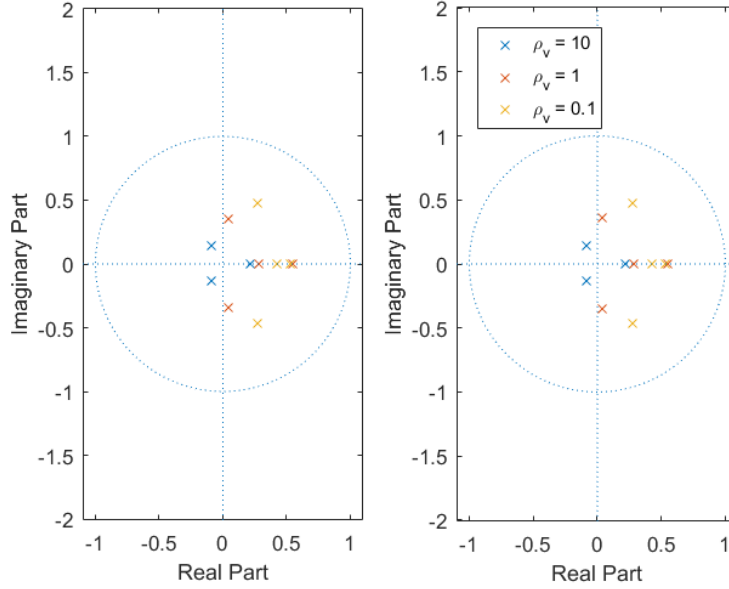


Figure 20: Pole locations for varying ρ_v using method 1. Open-loop system at left and closed-loop at the right.

Having in mind that the observer response settling time should be 2 to 10 times inferior to the controller response (the controller should never wait for the estimator) we selected $\rho_v = 1$. This setup provided a response approximately 4 times faster than the LQR response of the previous section. Performing the same analysis on method 2 yields figure 21.

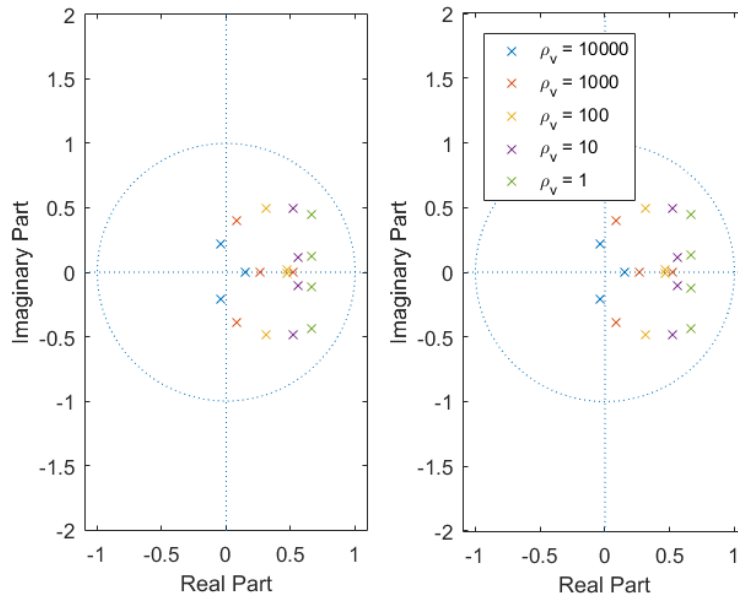


Figure 21: Pole locations for varying ρ_v using method 2. Open-loop system at left and closed-loop at the right.

To achieve the same results of method 1 we had to go one order of magnitude higher. With $Q_w = 1$, the chosen ρ_v was 1000, the absolute maximum order of magnitude we dimmed acceptable to have a viable design. In both cases the closed-loop poles are consistent. Examining closely the poles (take the conjugated left most ones for example), they are not identical in the two previous figures, which explains the slight variation observed in the time responses.

In method 1 the current estimator $M = [73.4204 \ 46.9067 \ 25.1685 \ 12.2572]^T$ and in the second method $M = [73.2086 \ 46.7468 \ 25.3937 \ 12.8373]^T$.

Our choice fell on the design through method 1 as it provided good results while maintaining relatively low parameter values.

2.4 Linear-Quadratic-Gaussian Controller Structure

The LQG controller is obtained by coupling a LQ controller with a Kalman filter and replacing the state by its estimate, that is to say, replacing 3 by

$$u(k) = -K\hat{x}(k). \quad (14)$$

Computing the joint system/controller dynamics we arrive at the block diagram in figure 22.

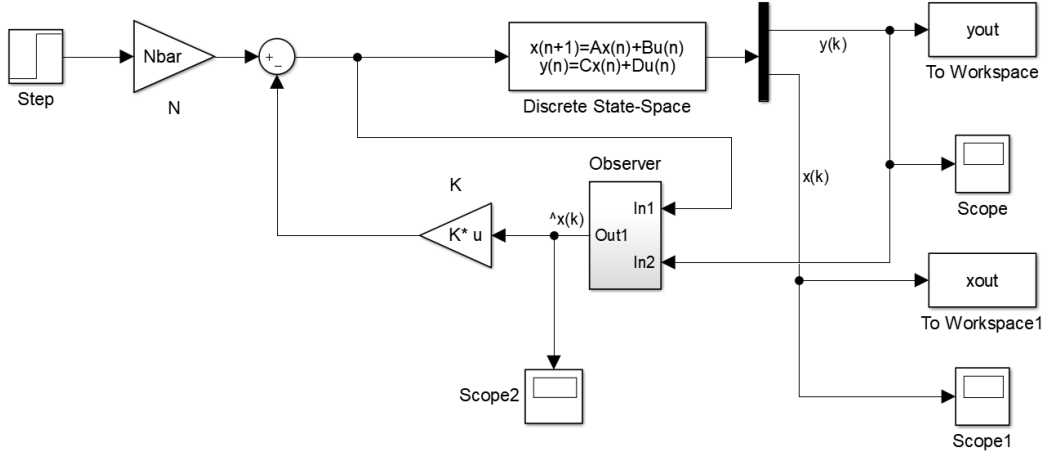


Figure 22: Joint system.

Following the state-space model to compute the loop transfer function, we obtain figure 23 using the loop-gains from methods 1 and 2.

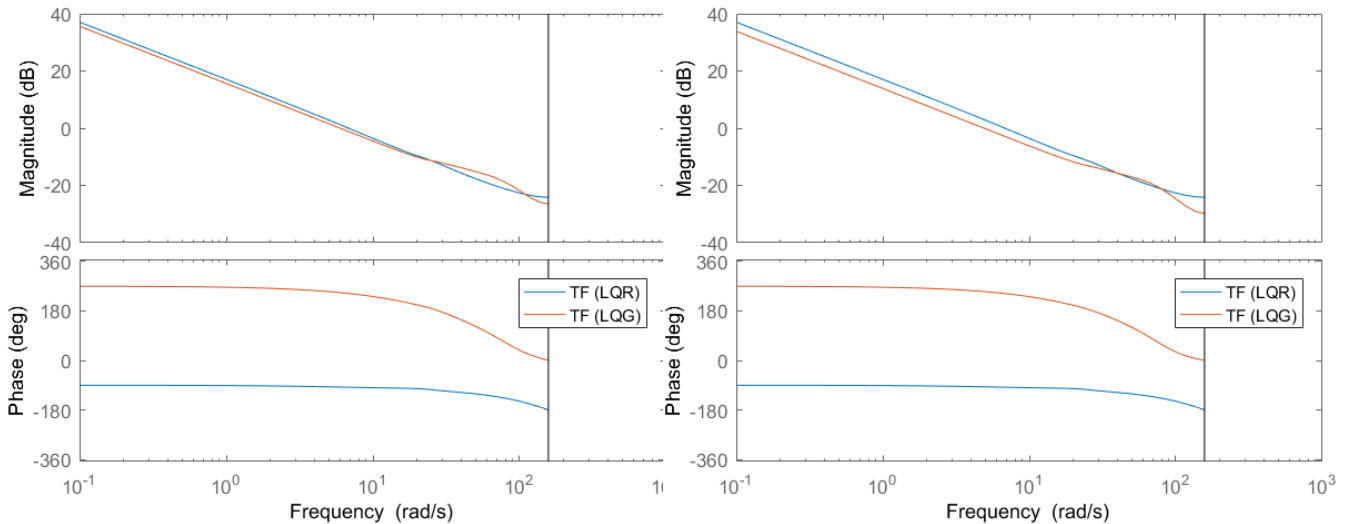


Figure 23: Open-loop transfer function using method's 1 (left) and method's 2 loop-gains (right).

Adding an external reference input we provide the closed-loop transfer function frequency response in figure 24. Both with method 1 and method 2, the responses of the LQR and LQG match. We reinforce that the pre-filter allows for the responses to have the same magnitude, making the joint system follow exactly the dynamics of the controller.

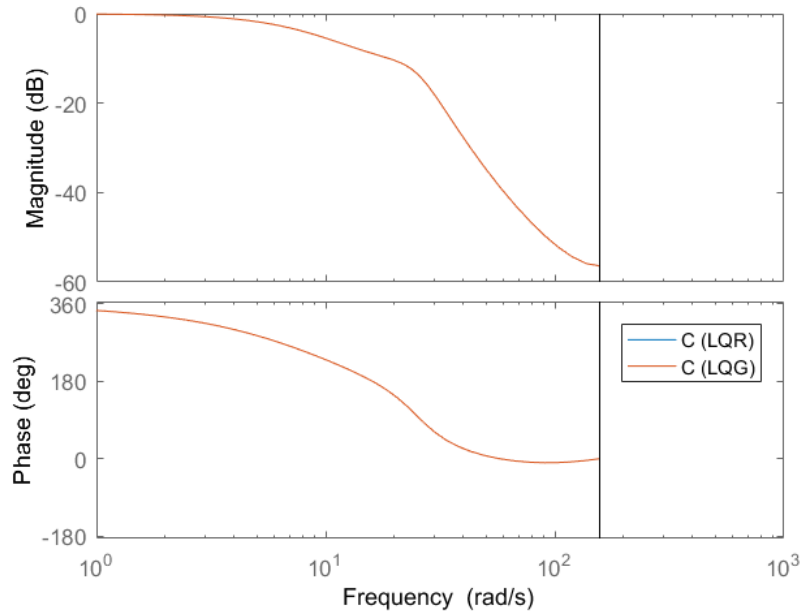


Figure 24: Closed-loop frequency response comparison between LQR and LQG controller.

By analysing what is happening in the complex plane we check the separation principle for pole locations in figure 25.

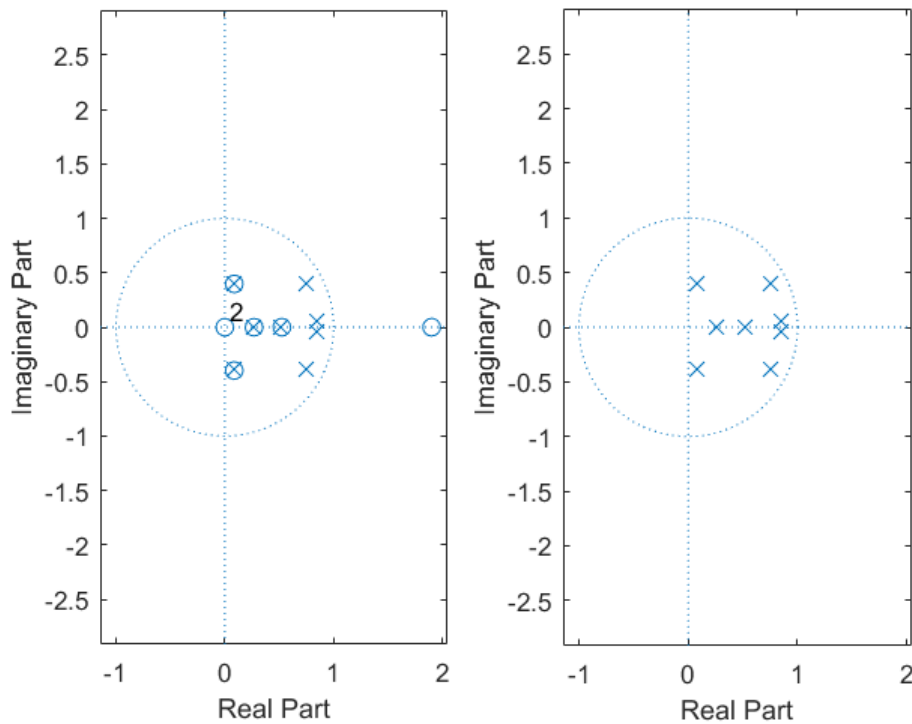


Figure 25: Closed-loop pole cancellation (left) and linear state feedback and estimator poles (right) for $Q_w = 100I$ and $R_v = 1$.

Repeating the root-locus analysis performed before we get figure 26.

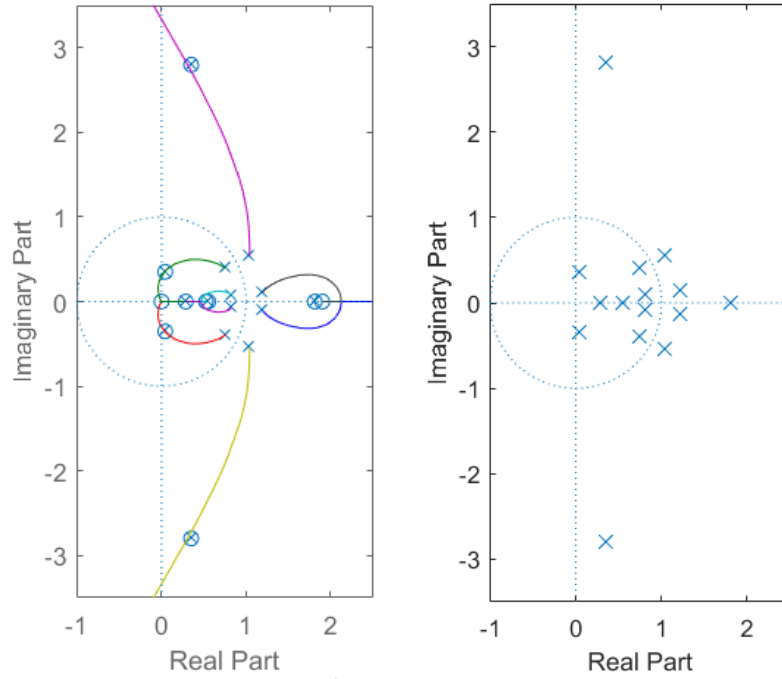


Figure 26: Root-locus analysis (left) and symmetric poles for $Q_w = 100I$ and $R_v = 1$ (right).

Comparing the left pole-zero plot of figure 26 with the one obtained earlier for direct state feed-back it is visible how it approximates it through selective pole-zero cancellations (figure 27).

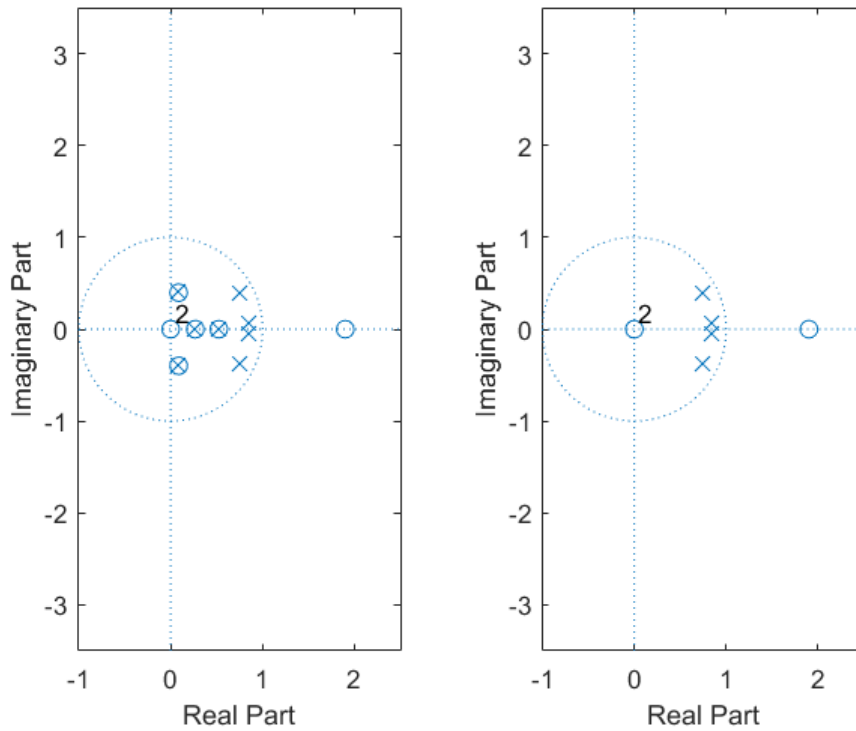


Figure 27: Closed-loop LQG pole cancellation (left) and closed-loop LQR (right).

3 Experimental Results

In this section, and using the LQG controller of the plant, a record of a set of identification experiments that show that the selected controller is the best choice is presented. Figure 28 has the block diagram used to perform the tests in the real plant.

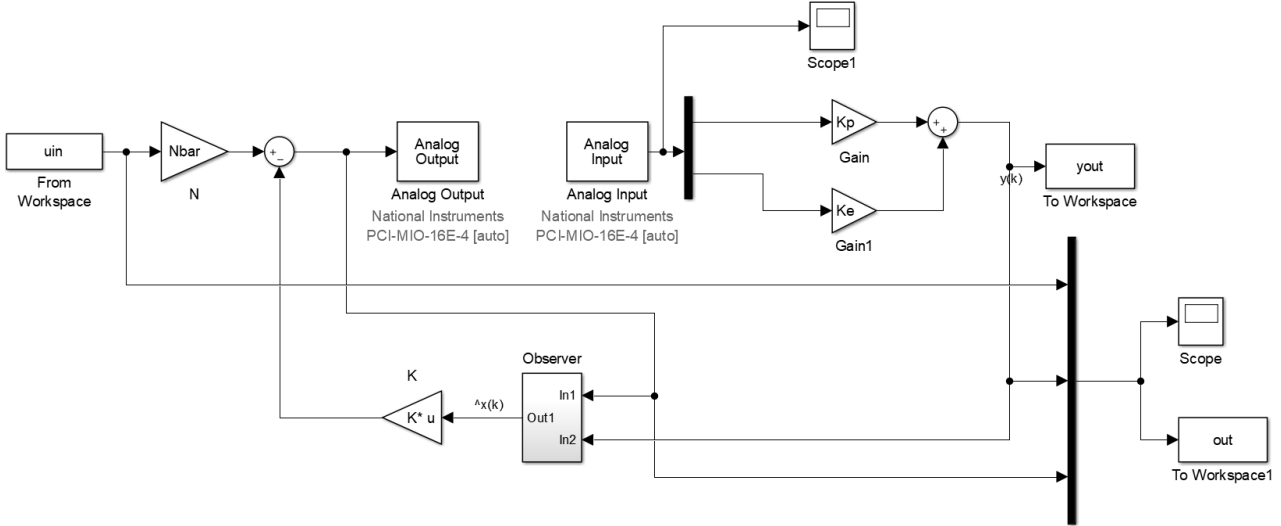


Figure 28: Diagram used on the real plant tests.

With our design we aimed at providing a solution that follows the input signal viably, and that could react to disturbances quickly and with minimum oscillations. Throughout the series of tests the limitations imposed by the dead zone were visible, as the motor could not precisely keep up with the reference signal as it could not nullify very small differences. Our design is showcased in the following figures and in three short videos referenced in this section and made available online.

Figure 29 has the response of the plant to a square signal without and with perturbances. The responses were recorded using parameters $Q_w = 100I$, $R_v = 1$ (LQE) and $R = 100$ (LQR). Video showcasing the response in the laboratory can be found here. The response with perturbances is here.

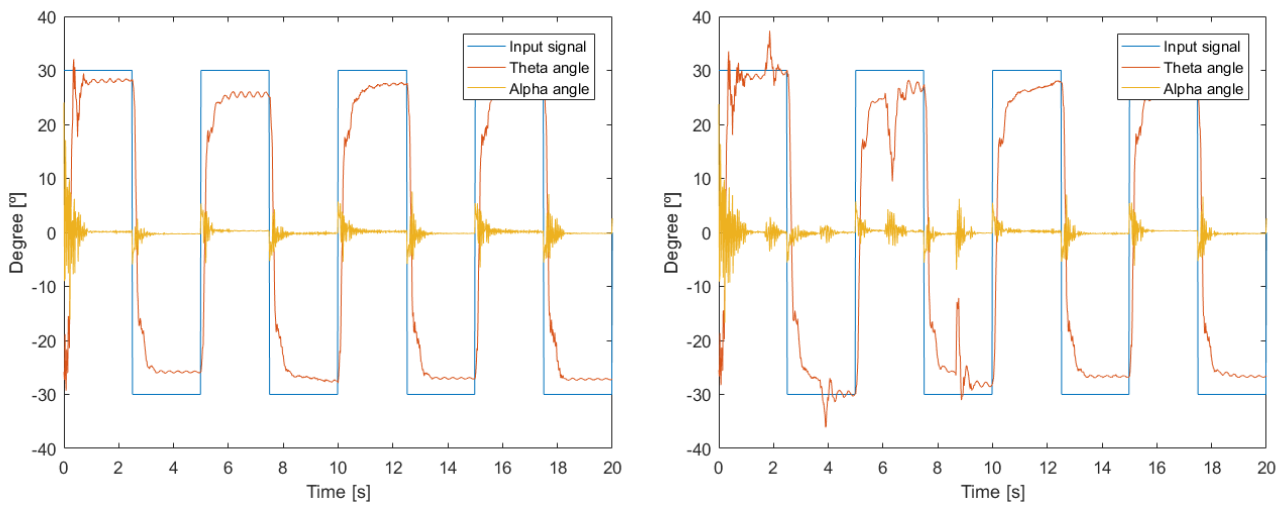


Figure 29: Square signal response with frequency of 0.2 [Hz], with parameters $Q_w = 100I$, $R_v = 1$ (LQE) and $R = 100$ (LQR). Response without perturbances (left) and with perturbances (right).

We observe a quick responding system that deals well with perturbances. In figure 30 we visualize under the same parameters the response to a signal with a frequency three times superior to the last one.

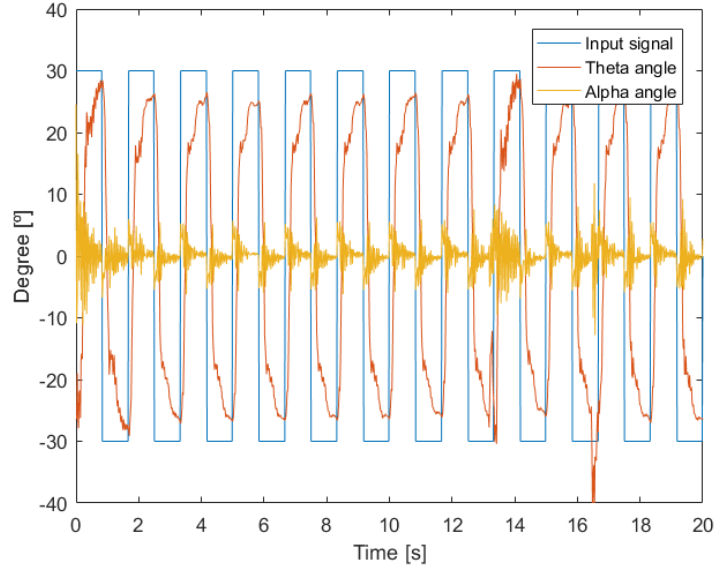


Figure 30: Square signal response with a frequency of $0.6 [Hz]$.

It can be seen that under this frequency the bar tip angle never stabilizes as the input signal changes polarization just as the output of the plant starts to converge to a stationary region - this indicates a limit in our solution as we cannot tolerate a higher frequency input signal if we want a response that goes with our desired performance goals (fewest oscillations as possible).

Changing the R to a more conservative value of 200 we obtain in figure 29 a steadier and slower convergence, as well as a less convincing perturbation response, as expected.

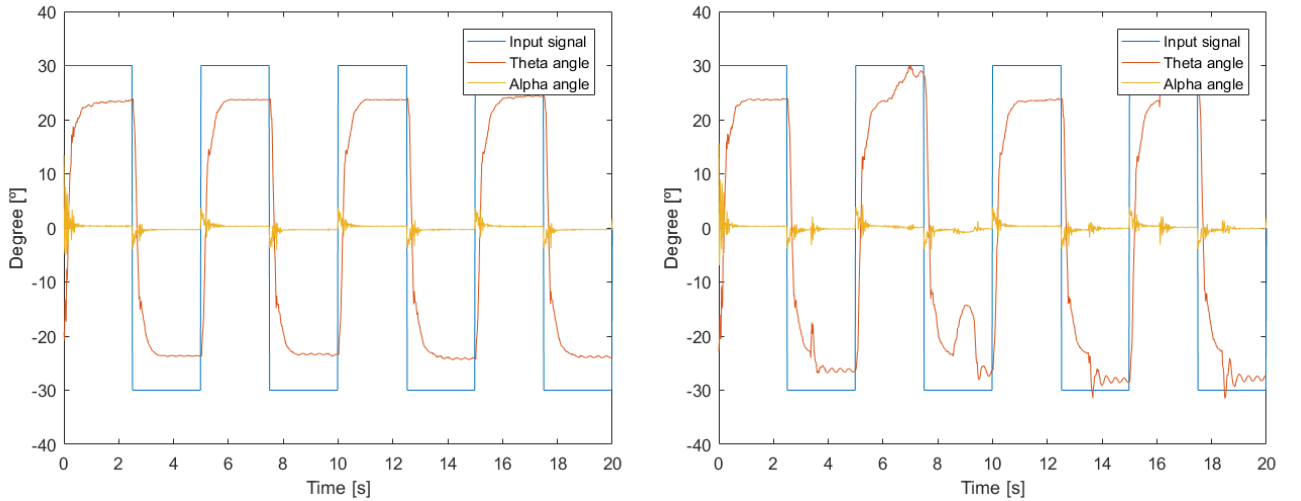


Figure 31: Square signal response with $Q_w = 100I$, $R_v = 1$ (LQE) and $R = 200$ (LQR). Response without perturbances (left) and with perturbances (right).

To evaluate the importance of the observation noise we raise the parameter R_v to 20.

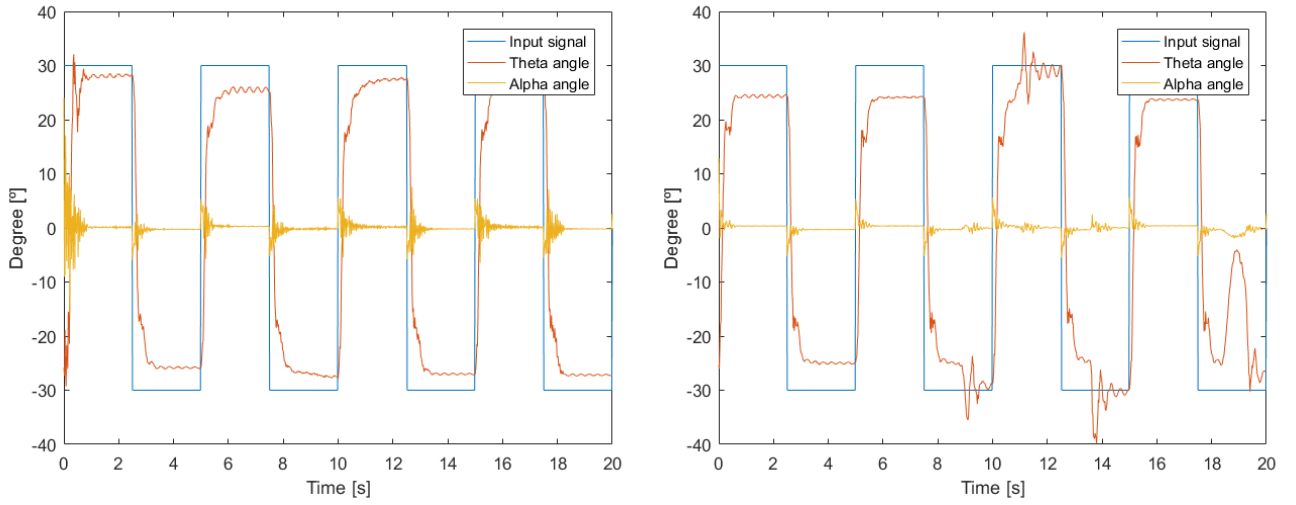


Figure 32: Square signal response with $Q_w = 100I$, $R_v = 20$ (LQE) and $R = 100$ (LQR). Response without perturbances (left) and with perturbances (right).

Because we made the assumption that the sensor provided noise the modeled system contraries this and the gains are changed to attenuate the oscillations present. Through inspection we do see that the bar tip angle is smoothed, comparing to the original experiment, confirming that the output yielded reacts as expected to the change of the observation noise.

In the last experiment we sent through a sawtooth input signal to further validate our work. The response obtained in the laboratory is shown here.

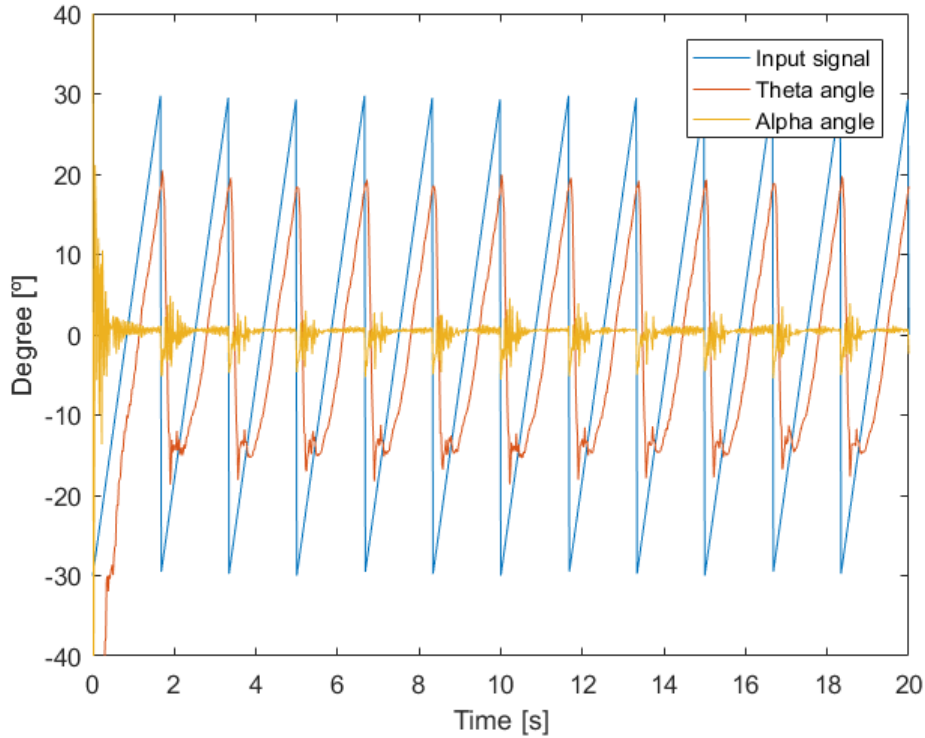


Figure 33: Sawtooth signal response with $Q_w = 100I$, $R_v = 1$ (LQE) and $R = 100$ (LQR).

3.1 Dealing with the Dead Zone

In order to surpass the dead zone limitation of the motor the block diagram in figure 34 was made.

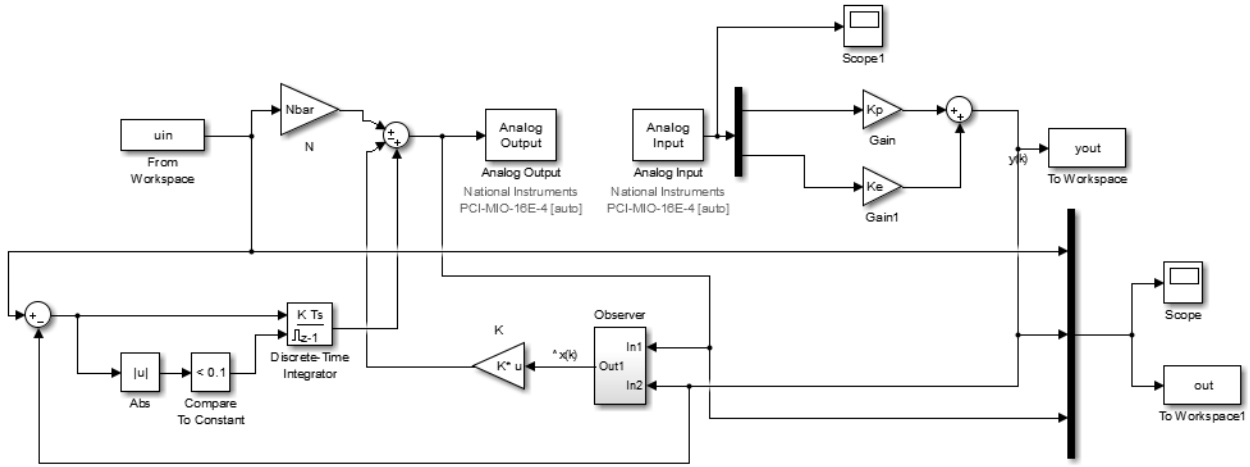


Figure 34: Simulink diagram able to deal with the dead zone imposed by the motor.

Comparing with the previous diagram at figure 28, we introduced a term at the input that takes into account the difference between the reference and the output. This difference is integrated through time, characterized by a constant parameter τ that is required to be adjusted and optimized according to our needs. We set the integrator's reset value at 0.1, indicating that any error below that absolute value will be excluded from the additive term and will thus not count towards our system's behavior. This calibration process of defining τ is done by inputting a step signal long enough to allow the integrator term to take effect.

Figure 35 showcases the system's time response to several τ constants.

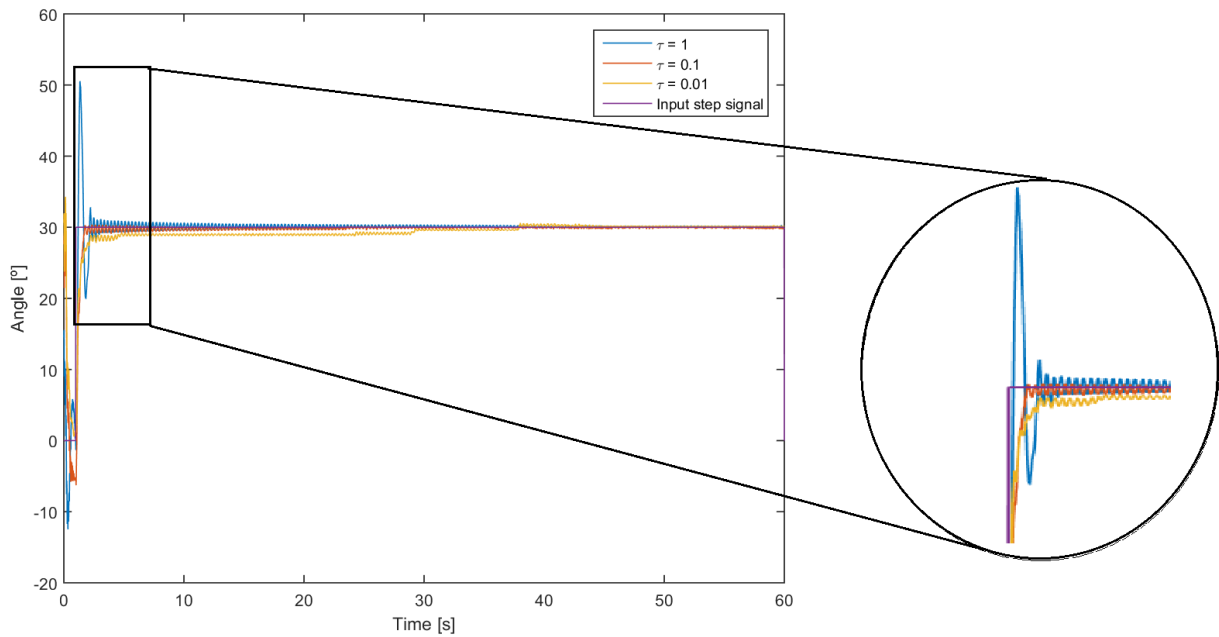


Figure 35: System's time response to step signal, with varying τ .

Our final parameter τ assumed value 0.1, as it was not big enough to cause overshoot in the output signal (as seen with $\tau = 1$), and not small enough for the response to take a long time to act (as seen with $\tau = 0.01$). The reset interval proved to be extremely efficient in maintaining a system whose response was already close to the desired value, to continue close to the reference (without this reset a good signal would sometimes be somewhat distorted due to the accumulated error of very small errors).

Maintaining parameters $Q_w = 100I$, $R_v = 1$ (LQE) and $R = 100$ (LQR), and repeating the square signal test (figure 36) and the sawtooth test (figure 37) we analyze the efficacy of our adaptation. We changed the frequency from the last batch of experiments to 0.05 Hz.

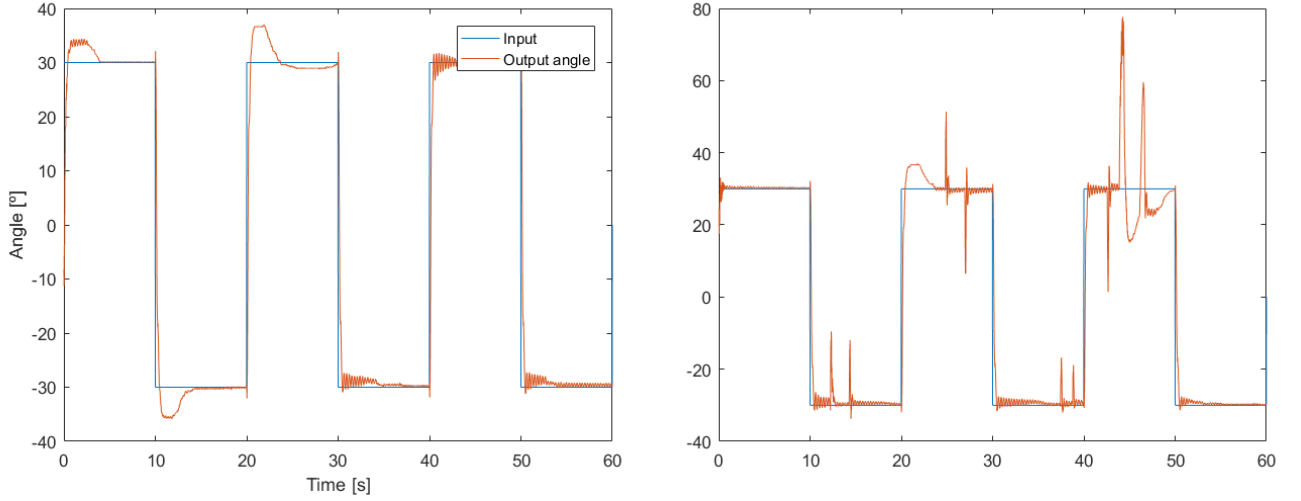


Figure 36: Time response to square signal, dealing with dead zone with $\tau = 0.1$. Signal without perturbances (left) and with perturbances (right).

The inclusion of the integrator proved inconsistent as some overshoot was introduced in certain parts of the signal. Further tuning should be done to prevent this effect.

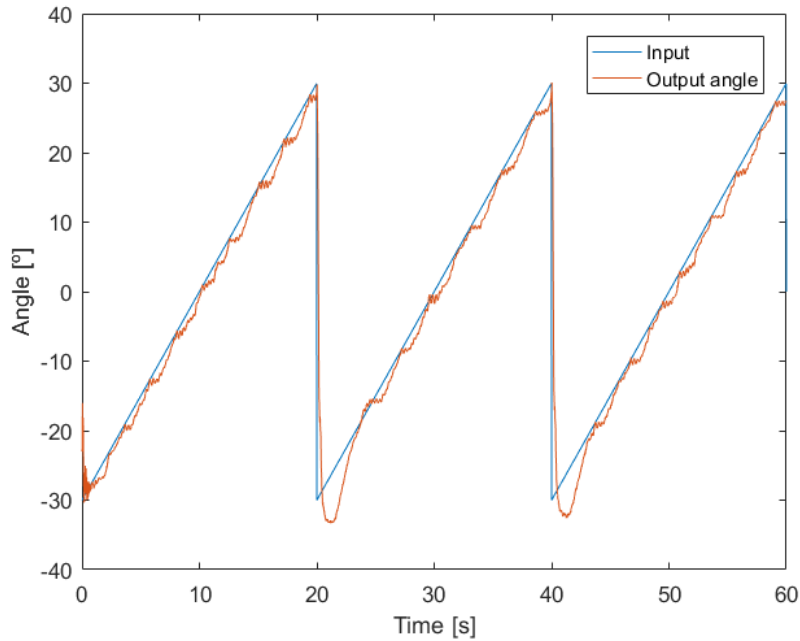


Figure 37: Time response to sawtooth signal without perturbances, dealing with dead zone with $\tau = 0.1$.

In the case of the sawtooth, the integrator reduces significantly the error between the reference and the output (comparing to figure 33), but its reset level disrupts the smooth following of the target signal because, as it resets, the input value becomes insufficient for the excitation of the motor (dead zone).

Withdrawing the reset from the block diagram (figure 38), the system's response becomes much better for non-stationary references.

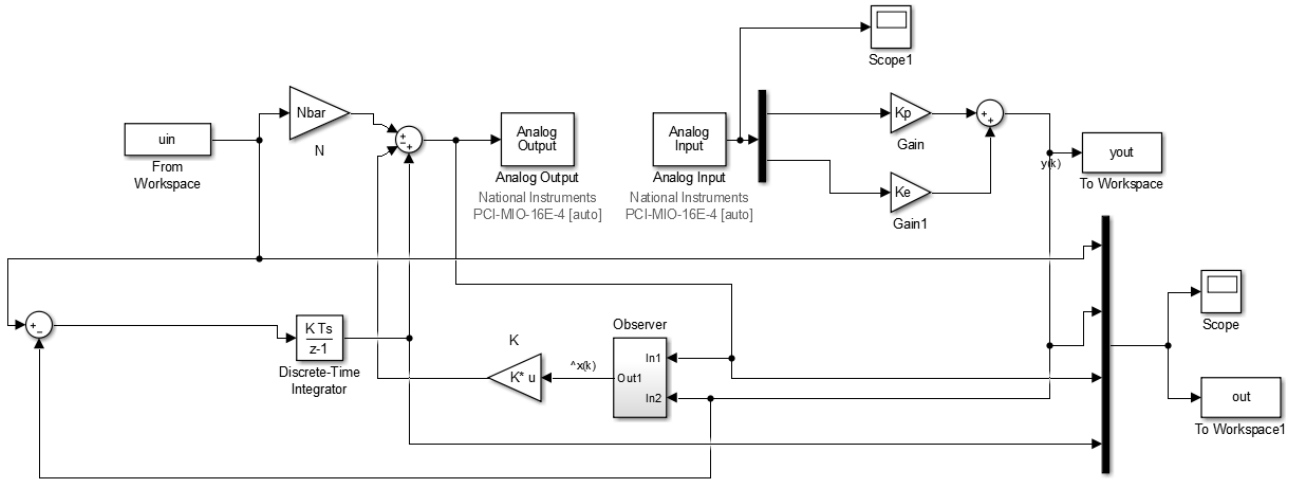


Figure 38: Joint system without reset level on the integrator.

Figure 39 reveals the tests of the square and sawtooth signal in this new setup. A video showcasing the response in the laboratory of the last can be found [here](#).

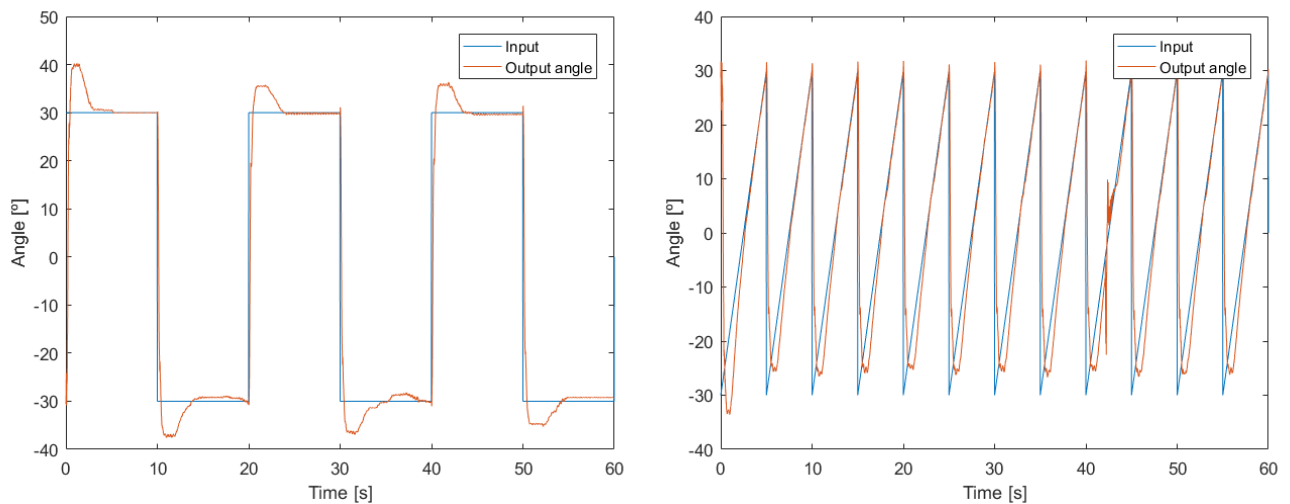


Figure 39: Time response to square signal without perturbances (left) and to the sawtooth signal with one perturbation (right) without the integrator's reset, with $\tau = 0.1$.

We conclude that the reset pays off when we encounter a stationary reference for prolonged periods of time as it assumes very small errors are caused by the normal oscillations of the system, therefore it does not integrate them. Otherwise, on non-stationary references, we assume these errors do not play a big enough part on the tracking error and so we take into account every discrepancy.

To develop a more robust system we add a selector portion to the simulink (figure 40). The reset now only takes action when the signal is stationary (null derivative) and the error exceeds the threshold of 0.1, combining the best of the two setups we tested before (integrator with and without reset).

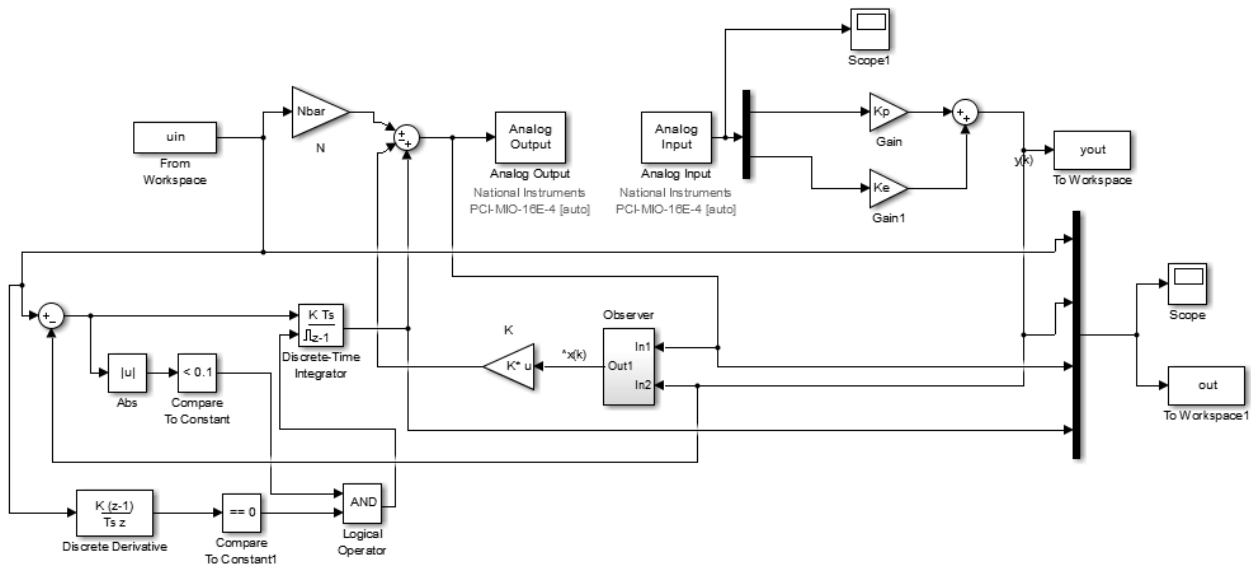


Figure 40: Robust system with selector of reset level.

To accommodate non-stationary, with non-zero acceleration another integrator should be added to the system.